Crucial role of *d-d* Coulomb correlations in the magnetocaloric ferrimagnets Gd$_6$(Mn$_{1−x}$M$_x$)$_{23}$ (M = Fe, Co)

T. Ly Nguyen [1,2] Chueh-Cheng Yang,[3] Chia-Hsin Wang,[1] Yaw-Wen Yang,[1] Th. Mazet [4] E. Gaudry [4] D. Malterre,[4]
M. Yoshimura [1] Y. F. Liao,[1] H. Ishii [1] N. Hiraoka,[1] H. J. Lin,[1] Y. C. Tseng,[2,3] and A. Chainani [1]

[1]*National Synchrotron Radiation Research Center, Hsinchu 30076, Taiwan*

[2]*International College of Semiconductor Technology, National Yang Ming Chiao Tung University, Hsinchu 30010, Taiwan*

[3]*Department of Materials Science and Engineering, National Yang Ming Chiao Tung University, Hsinchu 30010, Taiwan*

[4]*Université de Lorraine, CNRS, Institut Jean Lamour, F-54000 Nancy, France*

It is well-known that in elemental metals, the onsite Coulomb energy of transition-metal (TM) *d*-electrons, U_{dd}, is significantly smaller than U_{ff} of *f*-electron rare-earth (RE) metals. Consequently, U_{dd} is often neglected in RE-TM intermetallic alloys. In spite of the low value of U_{dd} compared to U_{ff}, we quantify and clarify the important role of U_{dd} in partially filled *d*-bands of RE-TM alloys. We investigate the electronic structure of a typical RE-TM ferrimagnetic series Gd$_6$(Mn$_{1−x}$M$_x$)$_{23}$ (M = Fe, Co; $x = 0.0, 0.3$), which shows promising magnetocaloric properties. Resonant photoemission and constant initial state spectroscopy is used to identify the Mn 3*d*, Fe 3*d*, and Co 3*d* partial density of states (PDOS) in the valence band. The photon energy-dependent spectral evolution allows us to separate out the lower Hubbard band and the two-hole correlation satellites in the Mn, Fe, and Co 3*d* PDOS. Using the Cini-Sawatzky method, we determine an average $U_{dd} = 2.1 \pm 0.4$ eV, 2.2 ± 0.4 eV, and 2.9 ± 0.4 eV for the Mn 3*d*, Fe 3*d*, and Co 3*d* states, respectively. The relatively larger U_{dd} for Co compared to Fe 3*d* states results in lower DOS for the coherent feature at the Fermi level (E_F) and higher DOS in the lower Hubbard band away from E_F in Gd$_6$(Mn$_{0.7}$Co$_{0.3}$)$_{23}$ compared to Gd$_6$(Mn$_{0.7}$Fe$_{0.3}$)$_{23}$. To understand the role of Coulomb correlations on the electronic structure and magnetic properties, *ab initio* electronic structure calculations using density functional theory with onsite Coulomb correlations (DFT+U) were carried out for the parent Gd$_6$Mn$_{23}$. The results show that the calculated Mn magnetic moments are consistent with experiments when $U_{Mn}^{DFT} = 0.75$ eV, corresponding to $U_{dd} = 1.65$ eV and $J_{dd} = 0.9$ eV. Further, using the calculated Gd and Mn PDOS and known photoionization cross-sections, the simulated Gd$_6$Mn$_{23}$ spectrum is fairly consistent with the experimental valence band spectrum. The results indicate the crucial role of *d-d* correlations in the presence of large *f-f* correlations for tuning the electronic structure and magnetic properties of RE-TM intermetallics.

I. INTRODUCTION

Intermetallic alloys containing rare earths (RE) and transition metals (TM) have played a central role in the fields of heavy-fermions [1–3], non-Fermi-liquids [4], magnetic metals [2–6], magnetocaloric materials [7,8], etc. More recently, there is a resurgence of interest in RE-TM-based materials as they are increasingly used in phosphors, lasers, energy storage batteries, catalysts, etc., in addition to their use as permanent magnets, such as the well-known Nd-Fe-B and Sm-Co alloys [9].

The large variety of applications of RE-TM-based materials arise from the synergy between localized *f* electrons of REs and the delocalized *d* electrons of TMs. The localized *f* electrons exhibit large magnetic moments μ and spin-orbit coupling (SOC), negligible bandwidths (W), and weak intersite exchange (J) interactions [5,6]. In contrast, the delocalized *d*-electrons in intermetallics show a smaller μ and SOC, but larger W and J which determine the magnetic ordering temperature. In an isostructural RE-TM series, with RE varying from Ce-Yb for the same TM, the RE-TM exchange coupling is always ferromagnetic (FM) for light REs

and antiferromagnetic (AFM) for heavy REs, but varying TM can also result in a competition of FM versus AFM order [10,11]. Many studies have carried out first-principles local spin-density approximation electronic structure calculations, without and with onsite Coulomb energy (LSDA and LSDA + U, where U is the onsite Coulomb energy) [12–19] as well as dynamic-mean-field theory (DMFT) calculations for understanding the magnetism of RE-TM alloys [20].

Early electronic structure calculations on RE-TM intermetallics focused on only including U_{ff} and neglected U_{dd} [12–15,20]. However, a few recent calculations have employed U_{ff} and U_{dd} to understand material properties, such as *d*-electron correlations in Ce-skutterudites [16], maximal magnetization in SmCo$_{5−x}$Ni$_x$ [17], and high-spin polarization in CeMnNi$_4$ [18,19]. An early pioneering experimental study combining photoemission spectroscopy (PES) and inverse-PES (I-PES; also called bremhstrahlung isochromat spectroscopy) of the 4*f* RE metals showed that U_{ff} is large, varying from ∼6 ± 1 eV for Ce to Pm, to a maximum of ∼11 ± 1 eV for Eu and Gd, and then reduced again to ∼6 ± 1 eV for Tb to Yb [21]. A recent experimental study identified the role of *d*-electron correlations in the RE-TM
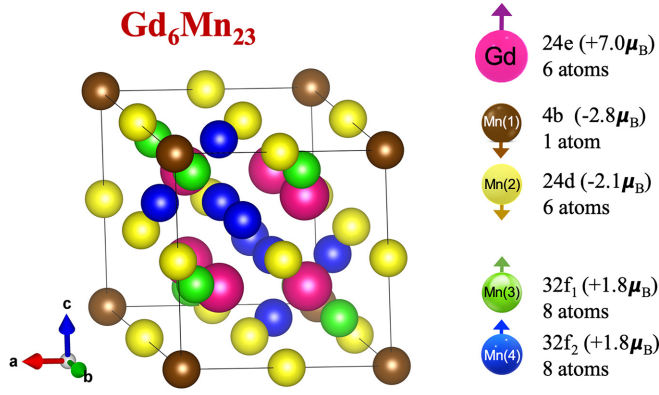
FIG. 1. The cubic crystal structure of Gd_6Mn_{23}

mixed-valence system $YbFe_2Al_{10}$ [22], although it was not quantified. Empirical formulas have been obtained for U_{ff} in RE metals because the experimentally obtained values are significantly smaller (due to solid-state screening) than U_{ff} values obtained from atomic calculations [23]. Similarly, empirical formulas as well as calculations for the elemental 3d TMs showed U_{dd} varying from ~1–3 eV for Ti to Ni [23,24]. These have been confirmed for the elemental TMs Mn-Ni by comparing LDA/LSDA+DMFT calculations with angle-resolved (AR)-PES experiments and are consistent with measurements of the two-hole final state Auger spectra which provide experimental estimates of U_{dd} [25–28]. More recently, since the discovery of superconductivity in the iron pnictides, the importance of strong correlations in metallic magnetic materials based on TMs has become well accepted [29–33]. Surprisingly, in spite of extensive studies, to date, there are no estimates of U_{dd} using the known experimental Cini-Sawatzky method [34–37] to quantify U_{dd} in RE-TM intermetallics. Since the localization-delocalization and magnetic properties arise from Coulomb and exchange correlations, we felt it is important to experimentally quantify element-specific onsite Coulomb correlations U_{dd} in the series $Gd_6(Mn_{1-x}M_x)_{23}$ (M = Fe, Co).

The intermetallic compounds RE_6Mn_{23} exhibits the Th_6Mn_{23} type cubic crystal structure (Fig. 1) and show interesting magnetic properties [38–45]. The RE_6Mn_{23} materials show a complex magnetic structure which was solved by polarized neutron diffraction studies of isostructural Y_6Mn_{23}. Delapalme *et al.* showed that the magnetic moments of Mn atoms on the b (~$-2.8\mu_B$) and d sites (~$-2.1\mu_B$) are oriented antiparallel to the moments of the f_1 (~$+1.8\mu_B$) and f_2 (~$+1.8\mu_B$) sites [42]. Thus, there are two types of Mn spin sites: up-spin "f_1, f_2" sites, and down-spin "b, d" sites in Y_6Mn_{23}. Applying the same Mn sublattice structure to Gd_6Mn_{23} in combination with magnetization measurements, it was shown that the localized Gd^{3+} spins are oriented parallel to the net Mn sublattice moments [42,46]. For Mn, as well as Fe and Co upon substitution, the magnetic moments indicate a high spin configuration which in turn suggests a small crystal field splitting and a larger exchange interaction [38–45]. More recently, the $Gd_6(Mn_{1-x}M_x)_{23}$ series has attracted attention for their magnetocaloric properties [46–49,54]. It is also known that the ferrimagnetic Curie temperature T_C and the bulk magnetization reduce upon

increasing the M content from $x = 0.0$ to 0.3 [41,44–47]. For $x = 0.0$, $T_C = 489$ K and it reduces to $T_C \sim 120$ K for $x = 0.3$ for both Fe and Co substitutions. A similar behavior is also seen in $Y_6(Mn_{1-x}Fe_x)_{23}$ [40,44,55,56] and suggests that T_C's of $Gd_6(Mn_{1-x}M_x)_{23}$ originate from the TM-sublattice. Magnetocaloric studies of Gd_6Mn_{23} revealed two maxima in the magnetic entropy changes (ΔS_M), a weaker maxima at $T = T_C$ and a stronger maxima at $T \sim 100$ K. The lower $T \sim 100$ K maxima increased with x and it was inferred that it could be due to Gd sublattice ordering or due to modifications in the magnetic structure for small $x = 0.0–0.2$ [47–49]. More importantly, the cooling or refrigeration capacity Q for $x = 0.2$ is significantly high at 3.4 J/cm^3 for $\Delta T = 10–300$ K with a magnetic field variation $\Delta H = 5$ T [47–49]. In comparison, the original giant magnetocaloric system $Gd_5Si_2Ge_2$ [57] shows a $Q = 3.6$ J/cm^3 but for a $\Delta T = 50$ K around T_C with $\Delta H = 5$ T. It was thus suggested that $Gd_6(Mn_{1-x}Fe_x)_{23}$ could be more suited for gas liquefaction applications [47–49].

In this work, we have carried out synchrotron induced resonant PES (RES-PES) and constant initial state (CIS) spectroscopy to identify the PDOS of Mn, Fe, and Co in the valence band of $Gd_6(Mn_{1-x}M_x)_{23}$ (M = Fe, Co; $x = 0.0–0.3$). We observe two-hole satellites which evolve from a resonant Raman satellite (RRS) to a normal Auger feature. This allows us to use the Cini-Sawatzky method [34–37] to estimate the average onsite Coulomb correlation energy U_{dd} for the Mn, Fe, and Co 3d PDOS. We obtain $U_{dd} = 2.1 \pm 0.4$ eV, 2.2 ± 0.4 eV, and 2.9 ± 0.4 eV for the Mn, Fe, and Co 3d states, respectively. In addition, based on the similarity of the 4f spectral feature in the valence band with known results of Gd metal, we estimate $U_{ff} \sim 11$ eV in the Gd 4f states [21,23]. The results show the importance of d-d correlations on the electronic structure and properties of $Gd_6(Mn_{1-x}M_x)_{23}$, and provide a quantification of average onsite U_{dd} for use in theoretical calculations which have not been reported for this series.

II. METHODS

A. Sample preparation and characterization

The $Gd_6(Mn_{1-x}M_x)_{23}$ with M = Fe, Co and $x = 0.0$ and 0.3, were synthesized using stoichiometric amounts of high-purity metals (Gd 99.9 wt.% from Rhodia, Mn 99.99 wt.% and Co 99.8 wt.% from Cerac, and Fe 99.8 wt.% from Alfa Aesar) by melting them in a high-frequency induction furnace (CE-LES) under pure argon atmosphere. The crystal structure was verified to be cubic by powder x-ray diffraction (Fig. 1), using a Philips X-Pert Pro Diffractometer, Cu Kα [47–49], and it confirmed the absence of impurity phases. The parent material Gd_6Mn_{23} showed a lattice parameter $a = 12.533(1)$Å, which decreased to $a = 12.335(1)$ Å for $Gd_6(Mn_{0.7}Fe_{0.3})_{23}$ and $a = 12.197(1)$ Å for $Gd_6(Mn_{0.7}Co_{0.3})_{23}$, as reported earlier [47–49]. The chemical purity and composition of each sample was checked by microprobe analysis (Cameca SX100) on mirror polished powder samples dispersed in a cold resin. The microprobe measurements indicate that, within the error bars (ca. 1 at%), the compositions of the alloys, taken from an average of six randomly chosen pinpoints, are homogeneous and identical to their nominal compositions.

B. Spectroscopy experiments

The soft-x-ray PES and CIS experiments were carried out at BL24A of the Taiwan Light Source using a linearly polarized photon beam with incident photon energies in the range of $h\nu = 600$–1000 eV. A liquid-N_2 flow-type cryostat was used to cool the samples down to $T = 140$ K. Samples were scraped in vacuum preparation chamber at 1×10^{-7} mbar, and immediately transferred to the connected main chamber at a ultrahigh vacuum of 8×10^{-10} mbar for measurements. The energy calibration and resolution($\Delta E = 0.5$ eV at $h\nu = 1000$ eV) were determined from the Fermi edge (E_F) spectrum of a gold foil mounted on the sample holder. XAS measurements were carried out using the total electron yield mode (TEY). RES-PES spectra were measured across the Mn 2*p*-3*d*, Fe 2*p*-3*d* and Co 2*d*-3*d* thresholds, and the spectra were normalized for scan time and incident photon flux. The hard x-ray PES (HAXPES) experiments were carried out at the Taiwan beam line BL12XU in SPring-8, Hyogo, Japan, with a total-energy resolution of 0.28 eV using linearly polarized photons. The sample was cooled using a liquid-N_2 flow-type cryostat. Samples were cleaved in the preparation chamber in a vacuum of 5×10^{-9} mbar and immediately transferred for measurements in the main chamber at $T = 80$ K at a vacuum of 5×10^{-10} mbar. The energy calibration and resolution were determined from the E_F spectrum of a gold film mounted on the sample holder. The HAXPES data were obtained in the angle-integrated mode with an incident photon energy $h\nu = 6.5$ keV. The surface contamination was monitored by O 1*s* and C 1*s* and the surfaces were clean and stable for 6 h for soft x-ray PES and more than 24 h for the HAXPES measurements. The TM 2*p* core-level spectra of Fe, Mn, and Co were analyzed using a least-squares fitting method to quantify peak-energy positions, shape and widths. A Shirley-type background with asymmetric Doniach-Sunjic (DS)-type Voigt profiles was found to be appropriate for all measured peaks reported in this study.

C. DFT+*U* electronic structure calculations

Electronic structure calculations were carried out for the parent Gd_6Mn_{23} using the Vienna ab-initio simulation package (VASP) [50–52] to obtain the PDOS and magnetic moments. The spin-polarized calculations were performed with the projector augmented wave (PAW) method using a plane-wave basis set [52]. We used the following electron configurations: $3p^6\ 3d^6\ 4s^1$ for Mn, and $5s^2\ 6s^2\ 5p^6\ 5d^1\ 4f^7$ for Gd. A structural optimization was performed within the GGA-PBE (Perdew-Burke-Ernzerhof) approximation which provided a cubic cell parameter a close to the experimental value: $a_{exp} = 12.54$ Å and $a_{cal} = 11.78$ Å. The calculations were performed for the optimized structure using the simplified (rotationally invariant) method to the DFT+U [53]. In this method, the onsite Coulomb (U) and Hund's exchange (J) interactions do not enter separately but only as a single parameter $U^{DFT} = U - J$. The parameters U_{Mn}^{DFT} was varied between 0.0 and 2.3 eV, while for Gd, U_{Gd}^{DFT} was varied from 6.0 to 12.0 eV to obtain magnetic moments close to the experimental values. The one-electron Kohn-Sham orbitals were expanded in a plane-wave basis set and the cutoff for the kinetic energy was 360 eV. The total energies were minimized until the energy differences between two electronic cycles were less than 10^{-4} eV. The reciprocal space integration was carried out with a Monkhorst-Pack k-point grid of $9 \times 9 \times 9$.

III. RESULTS AND DISCUSSIONS

A. Two-hole correlations and Mn 3*d* Hubbard band of Gd_6Mn_{23}

The results of Mn *L*-edge XAS, off- and on-resonant PES, and the CIS spectra, core-level and valence band PES of the parent material Gd_6Mn_{23} are shown in Figs. 2(a)–2(f). To carry out resonant PES data shown in Figs. 2(b) and 2(c), we first measured the Mn *L*-edge XAS spectrum shown in Fig. 2(a). The spectrum shows typical single peak features for the L_3 and L_2 edges at photon energies of $h\nu = 639.8$ eV and 651.1 eV, respectively, which match well with Mn metal spectrum [28]. The Mn metal type spectra was also confirmed by measuring the Mn 2*p* soft x-ray PES with a photon energy $h\nu = 1000$ eV as shown in Fig. 2(d). The Mn 2*p* spectrum consists of the $2p_{3/2}$ and $2p_{1/2}$ features at a binding energy (BE) of 638.4 and 649.7 eV. The Mn $2p_{3/2}$ and $2p_{1/2}$ features could be resolved into doublets and fitted with asymmetric Doniach-Sunjic line shapes, consistent with HAXPES results reported recently [58]. It was shown that the relative intensity of the doublets follows the Mn up-spin and down spin site occupancies which change systematically with Fe content x in $Gd_6(Mn_{1-x}Fe_x)_{23}$. We then measured the soft x-ray PES valence band [Fig. 2(e)] to characterize the energy range of the valence band features. The valence band spectra show the Gd 4*f* main peak at about 7.7 eV BE and a weak shoulder at ~8.8 eV which is attributed to surface feature as it is missing in HAXPES spectra shown in Fig. 4(c). Two additional features are observed, one at 0.5 eV BE which cuts the E_F and a broad feature with a peak at 2.7 eV BE. To establish that the 0.5 and 2.7 eV BE features originate from Mn, we measured the CIS spectra at 0.5 and 2.7 eV BE for $h\nu$ scanning across the Mn *L*-edge. The CIS spectra match well with the XAS Mn *L*-edge spectra as shown in Fig. 2(a) and confirm their Mn 3*d* character. The weaker intensity in the 0.5 eV CIS spectra is attributed to the admixture of Gd 5d states at and near E_F, as was discussed in HAXPES studies [58].

We then selected photon energies labeled A–I as shown in Fig. 2(a), and carried out valence band PES to investigate the Mn 2*p*-3*d* RES-PES behavior [Fig. 2(b)]. Focussing on the spectral features between E_F and 8.5 eV BE (just beyond the 4*f* peak), we observe systematic changes as a function of $h\nu$. As we increase $h\nu$ from A to E ($h\nu = 635.0$ to 638.3 eV) across the Mn L_3-edge threshold, we observe a systematic increase of the feature at 0.5 eV BE and a stronger increase of the feature at 3.3 eV BE [red dotted line in Fig. 2(b)] due to the Mn 2*p*-3*d* resonance effect. Furthermore, above incident $h\nu > 638.3$ eV, the high intensity feature at 3.3 eV BE moves to higher BEs (red full line). From photon energies F–I ($h\nu = 638.8$ eV to 642.8 eV), it systematically shifts to higher BEs from 3.7 to 7.8 eV BE. Since this feature tracks the changes in the photon energy, it arises from a two-hole correlation Auger satellite. To carefully determine the energy positions of this Auger feature, we plotted the difference spectra with respect to the off-resonant PES spectrum measured at $h\nu = 635$ eV, as shown in Fig. 2(c). The change in BE of this
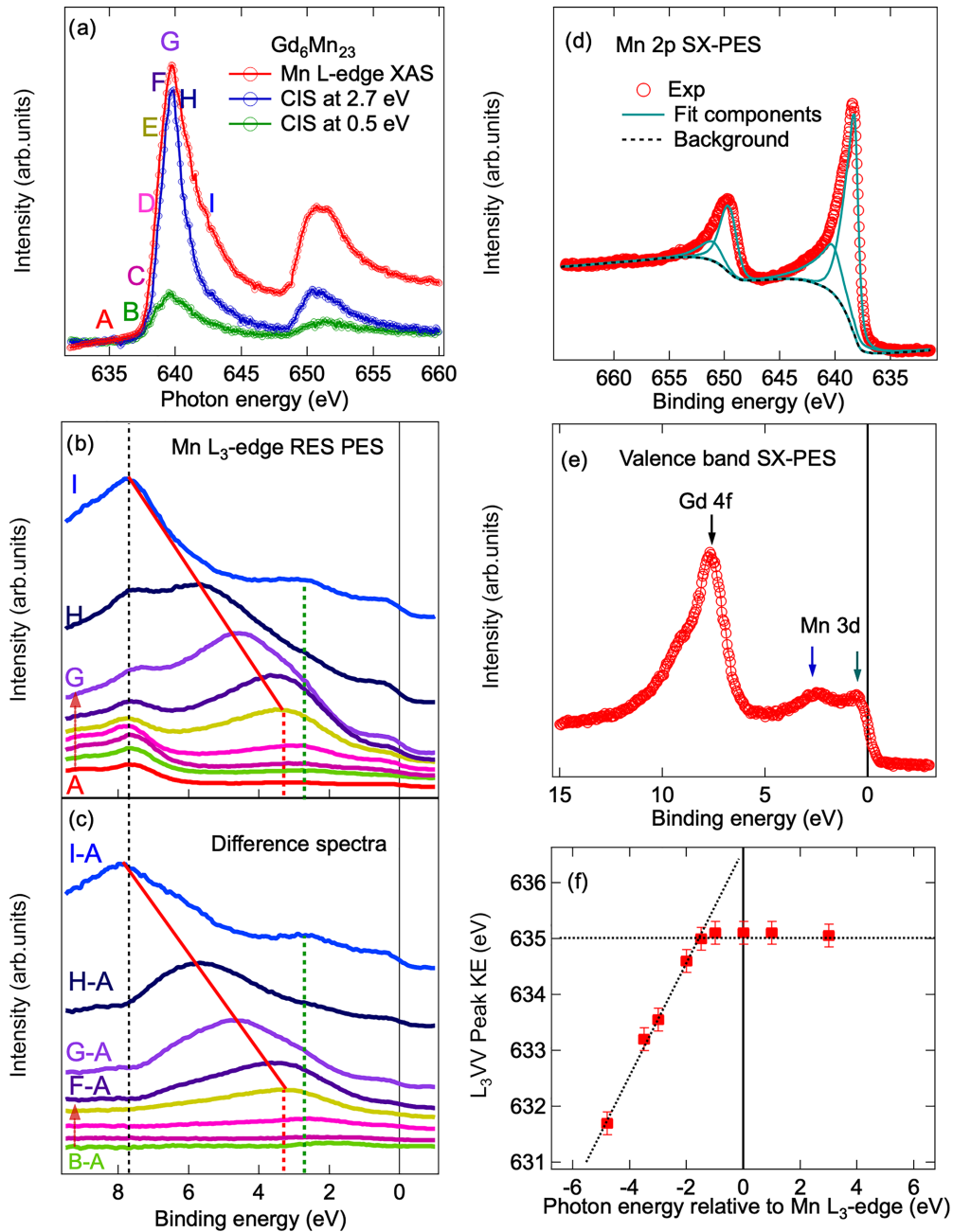
FIG. 2. (a) The Mn L-edge XAS and CIS spectra of Gd_6Mn_{23}. (b) Mn $2p$-$3d$ Res-PES spectra of Gd_6Mn_{23}. (c) Mn $2p$-$3d$ Res-PES difference spectra of Gd_6Mn_{23}. (d) The Mn $2p$ core-level SX-PES spectra of Gd_6Mn_{23} with photon energy $h\nu = 1000$ eV. (e) The valence band spectra of Gd_6Mn_{23} with $h\nu = 1000$ eV. (f) The plot of kinetic energy (KE) of the Auger L_3VV peak versus the incident $h\nu$ relative to the Mn L-edge XAS maximum energy. The intersection point of the two dotted straight lines corresponds to the crossover energy of the resonant Raman to normal Auger regime.

feature as a function of incident $h\nu$ with respect to the XAS main peak energy are plotted in Fig. 2(f). It confirms the two-hole correlation satellite exhibits a RRS to a normal Auger transition, i.e., it corresponds to the L_3VV Auger feature of Mn $3d$ character in the valence band DOS. This behavior matches well with Mn $2p$-$3d$ RES-PES of Mn metal which also showed a resonance at 3.3 eV BE [28].

Another important point to note is that at the highest photon energy shown in Fig. 2(b), the Mn $3d$ PDOS shows a broad feature spread between 1.5 and 3.5 eV, with a maximum at $\sim$2.7 eV (green dotted line), i.e., 0.6 eV below

the L_3VV Auger feature at 3.3 eV BE, just as is also seen in Fig. 2(e). This matches well with the lower Hubbard band of Mn metal reported earlier by Biermann *et al.* [25]. The authors carried out AR-PES of Mn metal for $h\nu = 14$–70 eV and showed that the $\sim$2.7 eV BE feature is dispersionless and matches well with the lower Hubbard band by comparing with LDA+DMFT electronic structure calculations. They also showed that the coherent quasiparticle feature was positioned within 0.5 eV BE. Thus, our results match closely with the coherent feature at 0.6 eV BE, the lower Hubbard band at $\sim$2.7 eV BE and the L_3VV Auger feature at 3.3 eV BE for Mn
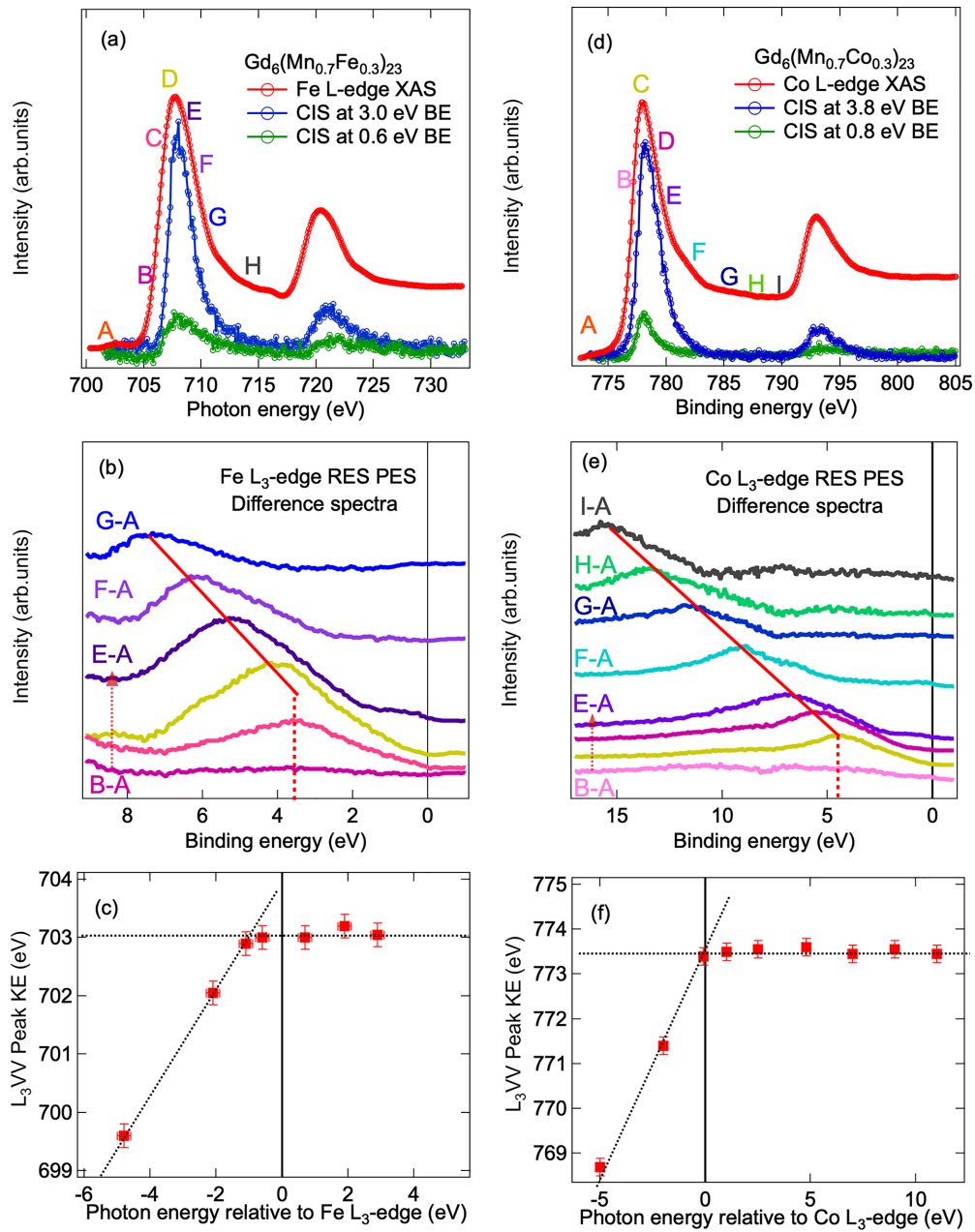
FIG. 3. (a) The Fe L-edge XAS and CIS spectra of $Gd_6(Mn_{0.7}Fe_{0.3})_{23}$. (b) Fe $2p - 3d$ Res-PES difference spectra of $Gd_6(Mn_{0.7}Fe_{0.3})_{23}$. (c) The plot of Kinetic energy (KE) of the Auger Fe L_3VV peak versus the incident $h\nu$ relative to the Fe L-edge XAS maximum energy. The intersection point of the two dotted straight lines corresponds to the crossover energy of the resonant Raman to normal Auger regime. (d) The Co L-edge XAS and CIS spectra of $Gd_6(Mn_{0.7}Co_{0.3})_{23}$. (e) Co $2p - 3d$ Res-PES difference spectra of $Gd_6(Mn_{0.7}Co_{0.3})_{23}$. (f) The plot of KE of the Co L_3VV Auger peak versus the incident $h\nu$ relative to the Co L-edge XAS maximum energy. The intersection point of the two dotted straight lines corresponds to the crossover energy of the resonant Raman to normal Auger regime.

metal, which is surprising as it suggests that the Mn $3d$ states in Gd_6Mn_{23} behave much like Mn metal.

B. Two-hole correlations of $Gd_6(Mn_{0.7}Fe_{0.3})_{23}$ and $Gd_6(Mn_{0.7}Co_{0.3})_{23}$

Next, we carried out similar experiments for the Fe $3d$ PDOS in $Gd_6(Mn_{0.7}Fe_{0.3})_{23}$. Figures 3(a)–3(c) show the Fe L-edge XAS and CIS, RES-PES difference spectra, and the plot of the BE of the Fe L_3VV Auger feature as a function of incident $h\nu$ with respect to the XAS L_3-edge peak energy.

Figure 3(a) shows that the Fe L-edge XAS is also like Fe metal with single peak features for the L_3 and L_2 at photon energies of $h\nu = 707.8$ eV and 720.5 eV, respectively. The spectra match well with Fe metal spectrum reported earlier [27]. The Fe $2p$ soft x-ray PES with $h\nu = 1000$ eV was also measured as shown in Supplemental Material [59] Fig. S1. It shows single peak Fe $2p_{3/2}$ and $2p_{1/2}$ features at a binding energy (BE) of 706.9 and 719.8 eV, and could be fitted with asymmetric Doniach-Sunjic line shapes, consistent with HAXPES results [58]. The peak positions and line shapes are consistent with Fe metal. The Fe L-edge CIS spectra of $Gd_6(Mn_{0.7}Fe_{0.3})_{23}$ was

FIG. 4. (a) Selected Fe L_3-edge spectra for incident $h\nu$ corresponding to off-resonance, on-resonance, and beyond on-resonance energy for $Gd_6(Mn_{0.7}Fe_{0.3})_{23}$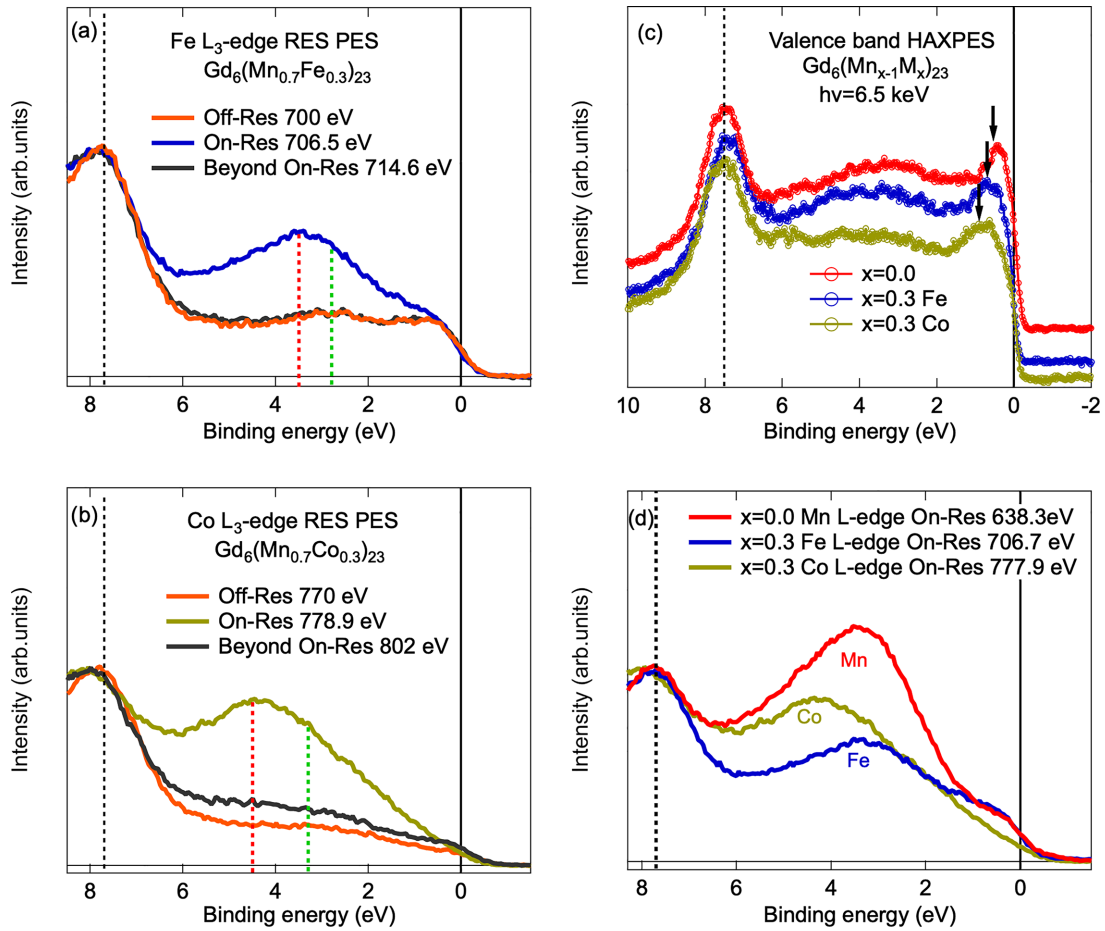. (b) Selected Co L_3-edge spectra for incident $h\nu$ corresponding to off-resonance, on-resonance and beyond on-resonance energy for $Gd_6(Mn_{0.7}Co_{0.3})_{23}$. (c) HAXPES valence band spectra of $Gd_6(Mn)_{23}$, $Gd_6(Mn_{0.7}Fe_{0.3})_{23}$, and $Gd_6(Mn_{0.7}Co_{0.3})_{23}$ measured with $h\nu = 6.5$ keV. (d) Comparative L_3-edge on-resonance spectra for Mn, Fe, and Co in the resonant Raman region, just before it becomes a normal Auger feature.

investigated at BEs of 0.6 and 3.0 eV and they match with Fe L-edge XAS as shown in Fig. 3(a). The Fe L_3-edge RES-PES difference spectra of $Gd_6(Mn_{0.7}Fe_{0.3})_{23}$ obtained from spectra measured at incident $h\nu = 701.7$–710.7 eV (labeled A–G) are shown in Fig. 3(b). Here again, we observe a systematic increase of the two-hole correlation satellite at 3.6 eV BE for $h\nu = 705.7$ and 706.7 eV (labeled B and C), and then from $h\nu = 707.2$–710.7 eV (D–G), the satellite shifts to higher BEs from 4.0 to 7.5 eV BE. The Fe $3d$ two-hole correlation satellite also exhibits a RRS to normal Auger transition as shown in Fig. 3(c).

Similarly, the corresponding experiments for the Co $3d$ PDOS in $Gd_6(Mn_{0.7}Co_{0.3})_{23}$ are shown in Figs. 3(d)–3(f). The Co L-edge XAS shows single peak features for the L_3 and L_2 at photon energies of $h\nu = 778.0$ eV and 793.0 eV, respectively, consistent with Co metal [60]. The Co $2p$ soft x-ray PES with $h\nu = 1000$ eV (Fig. S1 of the Supplemental Material) shows single peak Co $2p_{3/2}$ and $2p_{1/2}$ features at a binding energy (BE) of 778.0 eV and 793.0 eV, and could be fitted with asymmetric Doniach-Sunjic line shapes, again consistent with Co metal [61]. The Co L-edge CIS spectra of $Gd_6(Mn_{0.7}Co_{0.3})_{23}$ was investigated at BEs of 0.8 and 3.8 eV and they match with Co L-edge XAS as shown

in Fig. 3(d). The Co L_3-edge RES-PES difference spectra of $Gd_6(Mn_{0.7}Co_{0.3})_{23}$ obtained from spectra measured with $h\nu = 773.0$–789.0 eV (labeled A–I) are shown in Fig. 3(e). Here too, we see a systematic resonance of the two-hole correlation satellite, but at 4.4 eV BE for $h\nu = 776.0$ and 777.9 eV (labeled B and C), and then from $h\nu = 779.0$–789.0 eV (D to I), the satellite shifts to higher BEs from 5.5 to 15.5 eV BE. The Co $3d$ two-hole correlation satellite also exhibits a RRS to normal Auger transition as shown in Fig. 3(f). The enhancement of the correlation satellite of Co $3d$ PDOS is observed at a relatively higher BE of 4.4 eV compared to Mn and Fe $3d$ PDOS, which showed correlation satellites at 3.3 and 3.6 eV BE. Hence, we measured the variation of the Co two-hole satellite over a larger $h\nu$ range to clearly separate it from the Gd $4f$ feature at 7.7 eV BE.

In Figs. 4(a) and 4(b), we plot selected spectra for incident $h\nu$ corresponding to off-resonance, on-resonance (but in the resonant Raman region, i.e., just before it becomes a normal Auger feature and shifts in BE) and an energy far beyond resonance effects for $Gd_6(Mn_{0.7}Fe_{0.3})_{23}$ and $Gd_6(Mn_{0.7}Co_{0.3})_{23}$. The spectra are normalized at the Gd $4f$ peak (black dotted line). In $Gd_6(Mn_{0.7}Fe_{0.3})_{23}$, it is seen that the off-resonance and beyond resonance spectra shows Fe $3d$ features just below

E_F at a BE of 0.7 eV, and another broad feature at ~2.8 eV (green dotted line), which is below the on-resonance maximum correlation satellite feature at 3.6 eV BE (red dotted line). Following the analysis of the Mn $3d$ lower Hubbard band in Fig. 2, and the fact that the main Fe $3d$ bands of Fe metal occur at less than 1 eV BE in SX-ARPES spectra reported for Fe metal [26], we associate the 0.7 eV feature with the coherent Fe $3d$ band and the ~2.8 eV feature with the lower Hubbard band of Fe. For $Gd_6(Mn_{0.7}Co_{0.3})_{23}$, while there is small feature just below E_F at about 0.5 to 1 eV BE, there is another weak broad asymmetric feature between 2.0 and 4.5 eV BE. We tentatively assign the shoulder of this broad feature associated with the off-resonance feature at ~3.3 eV as the center of the weak lower Hubbard band (green dotted line), while the correlation satellite feature is at 4.4 eV BE (red dotted line). It is noted that the SX-ARPES of Co also showed that the main Co $3d$ bands lie below 1 eV BE [26], and no clear signature of the lower Hubbard band in Co has been reported to date.

Alternatively, using the Cini-Sawatzky method [34–37], we can estimate the onsite Coulomb energy U_{dd} for the Mn $3d$, Fe $3d$, and Co $3d$ states, from the L_3VV Auger features of our results. We use the equation which is valid in the Auger region, given by $U_{dd(A)} = E_{2p} - (h\nu - E_{LVV}) - 2\epsilon_{3d}$ [27], where E_{2p} is the BE of the M $2p$ main peak, $h\nu$ is the incident photon energy, and E_{LVV} corresponds to the BE of the Auger peak. In the equation, $2\epsilon_{3d}$ represents the average two hole energy without correlations. We use the BE of the coherent feature in the off-resonant spectra discussed in Figs. 2, 3(a), and 3(b) as a suitable measure of ϵ_{3d} because their Mn, Fe and Co $3d$ character was confirmed by the CIS spectra, respectively. We also used the HAXPES valence band spectra of $Gd_6(Mn)_{23}$, $Gd_6(Mn_{0.7}Fe_{0.3})_{23}$ and $Gd_6(Mn_{0.7}Co_{0.3})_{23}$ to obtain an independent measure of ϵ_{3d} [Fig. 4(c)]. The HAXPES spectra are normalized at the Gd $4f$ peak (black dotted line). Since Gd $5d$ cross-section is larger than Mn (5.5×), Fe (10×), and Co $3d$ (2×) at a high energy of ~8 keV, and smaller than Mn (7×), Fe (11×) and Co $3d$ (6×) at a low energy of 600 eV [62], the relative spectral intensities between E_F and 6 eV BE are enhanced in HAXPES compared to soft x-ray results shown in Figs. 2–4. However, the changes seen in the HAXPES spectra are attributed to the TM $3d$ states as the Gd $5d$ states usually have a large bandwidth of $\geqslant 5$ eV and a relatively small electron count ($\leqslant 0.3$ electrons) in Gd intermetallics [63–65], as is also obtained in our electronic structure calculations discussed later. As seen in Fig. 4(c), the main $3d$ band just below E_F is observed at 0.6 eV BE for $x = 0.0$, and it shows a slight shift to 0.7 eV for $x = 0.3$ Fe and gets rounded with weaker intensity at 0.8 eV for $x = 0.3$ Co. These values are close to the $\epsilon_{3d} = 0.5$, 0.6, and 0.8 eV from the off-resonant PES and the CIS spectra. Thus, the cross-sections indicate that the electronic states at E_F are dominated by the TM $3d$ states.

Using the above described equation for $U_{dd(A)}$, and values of ϵ_{3d}, E_{2p} and E_{LVV} obtained from HAXPES and the L_3VV Auger spectral analyses for several $h\nu$ values, we estimate the average onsite $U_{dd} = 2.1 \pm 0.4$ eV for Mn, 2.2 eV ± 0.4 eV for Fe and 2.9 ± 0.4 eV for Co. The detailed set of individual values for estimating the average onsite U_{dd} are listed

TABLE I. Comparison of magnetic moments (in μ_B) obtained with different values of U_{Mn}^{DFT} (in eV) and a fixed value of $U_{Gd}^{DFT} = 6.5$ eV, except the case when $U_{Mn}^{DFT} = U_{Gd}^{DFT} = 0.0$ eV. Values in square brackets are for Mn magnetic moments obtained from neutron diffraction (Ref. [42]).

U_{Mn}^{DFT}	0.0 eV	0.75 eV	1.5 eV	2.3 eV
Mn (4b) (μ_B)	-2.27	-2.96[-2.8]	-3.27	-3.53
Mn (24d) (μ_B)	-1.78	-2.57[-2.1]	-2.93	-3.30
Mn (32f$_1$) (μ_B)	+1.64	+1.87[+1.8]	+3.12	+3.42
Mn (32f$_2$) (μ_B)	+1.23	+1.76[+1.8]	+2.49	+2.83
net Mn/f.u. (μ_B)	+9.89	+10.58	+24.64	+26.68
/Mn atom (μ_B)	(+0.43)	(+0.46)	(+1.07)	(+1.16)
Gd/f.u. (μ_B)	+42.12	+43.08	+43.14	+42.84
/Gd atom (μ_B)	(+7.02)	(+7.18)	(+7.19)	(+7.14)
M_{Tot} (μ_B)	52.01	53.66	67.78	69.52

$M_{Tot} = 54.7 \mu_B$ from bulk magnetization for an applied field H = 5T (ref. 47). f.u.: formula unit.

with error bars in Table I of the Supplemental Material. It is also noted that the Gd $4f$ states are observed at a BE of 7.6 ± 0.3 eV for all the three cases of $x = 0.0$, 0.3 Fe, and 0.3 Co. As mentioned in the introduction, from a combination of valence band PES and conduction band I-PES, $U_{ff} \sim 11$ eV for Gd metal [21]. As seen in the HAXPES valence band spectra, the Gd $4f$ states are observed at the same BE in our results as in Gd metal, indicating $U_{ff} \sim 11$ eV for $x = 0.0$, 0.3 Fe, and 0.3 Co. In Fig. 4(d), we compare the on-resonance spectra in the resonant Raman region for $x = 0.0$, 0.3 Fe, and 0.3 Co with the spectra normalized at the Gd $4f$ peak (black dotted line). It is clearly seen that the spectral intensity of the Fe PDOS at and near E_F of the $x = 0.3$ Fe case is quite close to that of the Mn $3d$ PDOS of $x = 0.0$ parent, while the Co PDOS at and near E_F of the $x = 0.3$ Co case is significantly suppressed compared to the Mn $3d$ PDOS of $x = 0.0$ parent. Further, as shown in Supplemental Material Fig. S2, the Mn $3d$ PDOS of $x = 0.3$ Fe and 0.3 Co also shows the same behavior. Based on known theoretical results of DMFT calculations of the one-band Hubbard model [66] as a function of U/W, the observed spectral differences indicate that the TM $3d$ states in $Gd_6(Mn_{0.7}Co_{0.3})_{23}$ exhibit a larger U/W and are more strongly correlated compared to $Gd_6(Mn_{0.7}Fe_{0.3})_{23}$ $3d$ states.

To understand the relation of the $U_{dd(A)}$ estimated from experiment with the Hubbard onsite Coulomb energy $U_{dd(H)}$ between two d electrons (which corresponds to the 'process' $2M \rightarrow M^- + M^+$), we calculated the energies of the photoemission and two hole Auger final states for the d^n configuration. The photoemission final state spectrum corresponds to the process $d^n \rightarrow d^{n-1}$ while the Auger final state spectrum corresponds to the process $d^n \rightarrow d^{n-2}$. The photoemission and Auger spectra can be obtained easily in the limit of very small bandwidth W with respect to the Hubbard energy ($W \ll U_{dd(H)}$). In this limit, the electronic configuration is a pure d^n configuration with energy per atom:

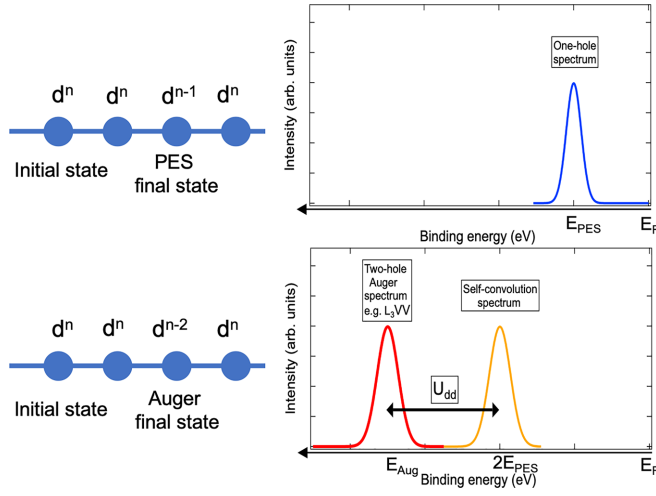$$E(d^n) = n\varepsilon_d + \frac{n(n-1)}{2}U_{dd(H)},$$

FIG. 5. Left: Final states of the photoemission (d^{n-1}) and Auger (d^{n-2}) process for the d^n initial state. Right: Schematic photoemission and Auger spectra. The blue spectrum is the photoemission (one-hole) feature at energy $E_{PES} = E(d^{n-1}) - E(d^n)$. The dark yellow spectrum centered at energy $2E_{PES}$ shows the self-convoluted PES feature and corresponds to two independent holes in the valence band. The red spectrum is the Auger spectrum with two onsite holes in the final state at an energy $E_{Aug} = E(d^{n-2}) - E(d^n)$.

where ε_d is the one-electron energy of a d state. In the photoemission process, one d electron is removed and the transition energy is given by

$$E_{PES} = E(d^{n-1}) - E(d^n) = -\varepsilon_d - (n-1)U_{dd(H)},$$

and a peak is expected at E_{PES} in the photoemission spectrum (see Fig. 5). The self-convolution of the photoemission spectrum shows a peak at an energy $2E_{PES}$ and represents two independent holes in the valence band. In the Auger process, the final state configuration of the photoexcited site is d^{n-2} and the Auger peak energy is given by

$$
\begin{aligned}
E_{Aug} &= E(d^{n-2}) - E(d^n) = -2\varepsilon_d - (2n-3)U_{dd(H)}, \\
U_{dd(A)} &= E_{Aug} - 2E_{PES} \\
&= -2\varepsilon_d - (2n-3)U_{dd(H)} - 2[-\varepsilon_d - (n-1)U_{dd(H)}] \\
&= U_{dd(H)}.
\end{aligned}
$$

A schematic picture describing this equivalence in the small bandwidth limit is shown in Fig. 5. To check this equivalence, it is important to compare the theoretically estimated $U_{dd(H)}$ values reported in the literature with the $U_{dd(A)}$ values obtained from the present experiments. If we consider, for example, the metal LVV Auger spectrum, it corresponds to an initial core hole in the L-edge and VV corresponds to two valence band holes in the final state. Then the energy of the two-holes on the same site in the Auger final state, $U_{dd(A)}$, compared to the self-convolution of the one hole photoemission spectrum, provides a measure of the onsite Coulomb energy (Fig. 5).

Using first principles LDA+DMFT calculations for a realistic five-band model and comparing with ARPES results, Biermann *et al.* [25] showed that $U_{dd(H)} = 3.0$ eV for Mn metal, while we obtain a value of $U_{dd(A)} = 2.1 \pm 0.4$ eV for
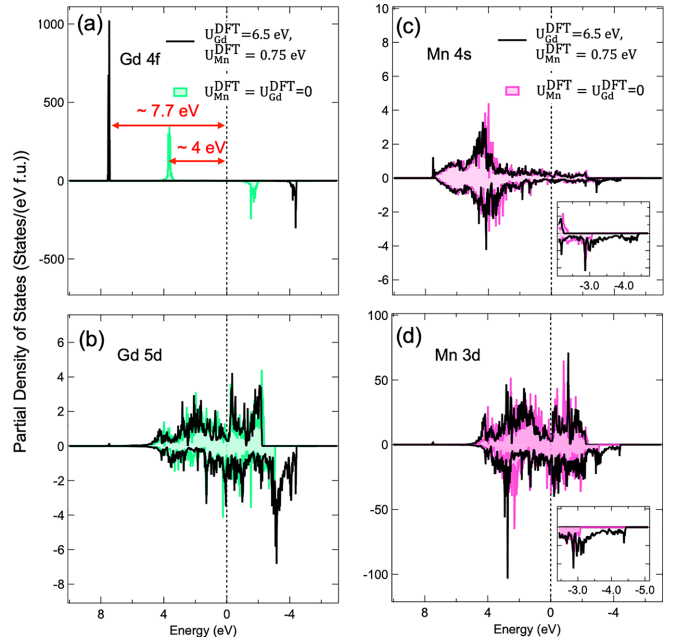

FIG. 6. The calculated PDOS of (a) Gd $4f$, (b) Gd $5d$, (c) Mn $4s$, and (d) Mn $3d$ for Gd_6Mn_{23}, showing the majority and minority spin states obtained from electronic structure calculations of Gd_6Mn_{23}. In each panel, the colored curves show the PDOS for $U_{Mn}^{DFT} = 0.0$ and $U_{Gd}^{DFT} = 0.0$, while the black curves show the PDOS for $U_{Mn}^{DFT} = 0.75$ eV and $U_{Gd}^{DFT} = 6.5$ eV. In panel (a), the Gd $4f$ states for $U_{Mn}^{DFT} = 0.0$ and $U_{Gd}^{DFT} = 0.0$ are seen at ~4 eV BE below E_F, while for $U_{Mn}^{DFT} = 0.75$ eV and $U_{Gd}^{DFT} = 6.5$ eV, the Gd $4f$ states are seen at ~7.7 eV BE below E_F. The insets in panels (c) and (d) show the corresponding differences on an expanded scale for Mn $4s$, and Mn $3d$ PDOS, respectively. Note the different y scales for all panels.

Mn in Gd_6Mn_{23}. However, using LSDA+DMFT calculations for Fe and Co metal and comparing with spin-resolved ARPES results, Sanchez-Barriga *et al.* [26] showed that $U_{dd(H)} = 1.5$ eV for Fe metal, and 2.5 eV for Co metal, while we obtain $U_{dd(A)} = 2.2 \pm 0.4$ eV for Fe in $Gd_6(Mn_{0.7}Fe_{0.3})_{23}$, and $U_{dd(A)} = 2.9 \pm 0.4$ eV for Co in $Gd_6(Mn_{0.7}Co_{0.3})_{23}$. The results indicate that $U_{dd(A)}$ in intermetallics are fairly close to the $U_{dd(H)}$ values estimated for elemental metals.

In Figs. 6(a)–6(d), we show the DFT+U spin-polarized generalized-gradient approximation (GGA) electronic structure calculations for Gd_6Mn_{23}. Each panel shows the calculations without onsite Coulomb energies, i.e., $U_{Mn}^{DFT} = 0.0$ and $U_{Gd}^{DFT} = 0.0$ (colored curves), compared with calculations with onsite Coulomb energies $U_{Mn}^{DFT} = 0.75$ eV and $U_{Gd}^{DFT} = 6.5$ eV. It can be seen in Fig. 6(a) that when $U_{Mn}^{DFT} = 0.0$ and $U_{Gd}^{DFT} = 0.0$, the Gd $4f$ states occur as a sharp feature at about 4 eV BE in the occupied states below E_F and nearly 2 eV above E_F. However, with $U_{Mn}^{DFT} = 0.75$ eV and $U_{Gd}^{DFT} = 6.5$ eV, the Gd $4f$ states occur as a sharp feature at about 7.7 eV BE in the occupied states and about 4.5 eV above E_F. For these values of U_{Mn}^{DFT} and U_{Gd}^{DFT}, we obtain the Gd and Mn magnetic moments in agreement with reported bulk magnetization [47], neutron diffraction [42] results. Table I shows the Mn magnetic moments obtained for different values of U_{Mn}^{DFT} varied from 0.0 to 2.3 eV, and the magnetic moments

from neutron diffraction (values in Table I square brackets) are consistent with those obtained for $U_{Mn}^{DFT} = 0.75$ eV. Here, $U_{Mn}^{DFT} = U_{Mn}^{eff} = U_{dd} - J_{dd}$ and assuming $J_{dd} = 0.9$ eV based on earlier work [67], the results imply that $U_{dd} = 1.65$ eV and is fairly close to the estimated $U_{dd(A)} = 2.1 \pm 0.4$ eV obtained from the Cini-Sawatzky method. As seen in Figs. 6(b) and 6(c), the Gd 5*d* and Mn 4*s* PDOS are relatively very weak compared to the Gd 4*f* states. The Gd 5*d* states plotted in Fig. 6(b) are spread from 5 eV BE below E_F to nearly 3 eV above E_F without U^{DFT}, but the minority states get shifted compared to the majority states with U^{DFT}. However, in Fig. 6(c), while the Mn 4*s* states are spread over a larger range from nearly 8 eV BE below E_F to nearly 3 eV above E_F without U^{DFT}, they also show a similar shift on including U^{DFT} [inset of Fig. 6(c)].

The Mn 3*d* PDOS show roughly $\sim$10 times higher weight compared to Gd 5*d* and Mn 4*s* PDOS, and are spread from 5 eV BE below E_F to nearly 3 eV above E_F when $U^{DFT} = 0$ [Fig. 6(d)], but they show a clear shift of the minority states compared to the majority states on including U^{DFT} [inset of Fig. 6(d)]. This leads to an increase in magnetic moments and gives values consistent with experiment. U_{Mn}^{DFT} was varied from 0.0 to 2.3 eV to obtain optimal magnetic moments as listed in Table I. The magnetic moment values obtained for $U_{Mn}^{DFT} = 0.75$ eV are quite close to the experimental values, while for $U_{Mn}^{DFT} = 0.0$ eV, the magnetic moments are smaller and for $U_{Mn}^{DFT} = 1.5$ and 2.3 eV, they are larger than the experimental values. It is noted that the Cini-Sawatzky method gives us a single broad Auger feature and consequently, a single value of $U_{dd(A)}$ for Mn with an error bar of ± 0.4 eV, although there are four types of Mn sites in Gd_6Mn_{23}. While the Mn magnetic moments can be clubbed into two types of Mn sites, two sites with up-spins and two sites with down-spins, nonetheless, it must be remembered that the Cini-Sawatzky method gives us an approximate value for the $U_{dd(A)}$ for all Mn sites. However, the electronic structure results are considered reliable because we get four different values of Mn magnetic moments for the four Mn sites, fairly consistent with values obtained from neutron diffraction (see Table I, values in square brackets) [42].

For the case of Gd magnetic moments, it is well-known that Gd 4*f* states behave like strongly localized Gd^{3+} $4f^7$ configuration with $S = 7/2$ in elemental Gd metal as well as in Gd alloys [63–65]. Early work on Gd metal showed that its ground state can be described by a single Slater determinant and a one electron DFT is valid [68,69]. It was shown that the average energies of the onsite Coulomb U_{ff} and exchange J_{ff} interaction could be calculated using the local spin-density approximation [68,69]. By comparing with the experimental N−1 and N+1 final states from photoemission and inverse-photoemission spectra of Gd metal [21], it was shown that $U_{ff} = 6.7$ eV and $J_{ff} = 0.7$ eV, and $U_{Gd}^{eff} = U_{ff} + 6J_{ff} \approx 11$ eV. Based on the Dudarev approach [53], $U_{Gd}^{DFT} = U_{ff} - J_{ff}$ was varied from 6.0 to 12 eV to obtain PDOS consistent with experiment. Using the obtained PDOS, we simulated the calculated valence band spectrum to compare with the experimental valence band spectrum [62]. The calculated spectrum was obtained by multiplying the PDOS with known photoionization cross-sections at 1000 eV [62] and convoluted with a Gaussian function (1.0 eV FWHM for
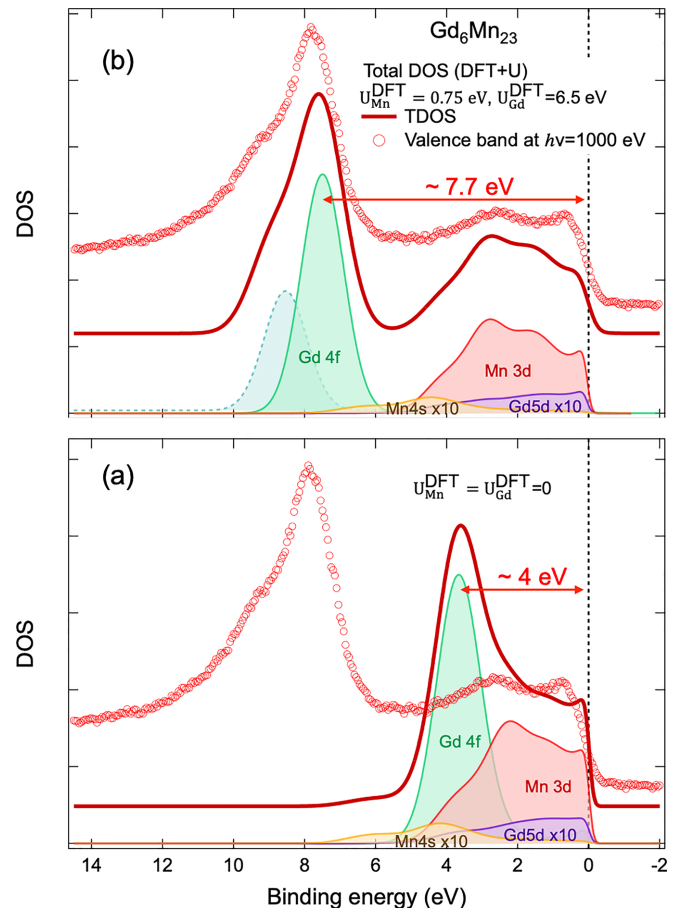

FIG. 7. Comparison of the calculated spectrum of Gd_6Mn_{23} with the experimental spectrum of Gd_6Mn_{23}. Panel (a) shows the spectrum simulated using PDOS obtained with $U_{Mn}^{DFT} = 0.0$ and $U_{Gd}^{DFT} = 0.0$. Panel (b) shows the spectrum simulated using PDOS obtained with $U_{Mn}^{DFT} = 0.75$ eV and $U_{Gd}^{DFT} = 6.5$ eV. The Gd 4*f* and Mn 3*d* occupied partial DOS show features consistent with the experimental spectrum. The weak shoulder at $\sim$8.8 eV BE is attributed to the surface Gd 4*f* states and is simulated as a replica of the main Gd 4*f* feature with reduced intensity. For soft x-ray PES, the Mn 4*s* and Gd 5*d* cross-sections are very weak and lead to very small intensities in the spectrum.

Mn 3*d*, Mn 3*s*, and Gd 5*d* PDOS; and 1.5 eV FWHM for Gd 4*f* PDOS). The results are shown in Fig. 7(a) for the case without onsite Coulomb energies, while Fig. 7(b) shows the calculations with onsite Coulomb energies and Hund's coupling.

It is clear that the calculated spectrum without onsite Coulomb energies does not match with the experimental spectrum, as shown in Fig. 7(a). However, based on the comparison shown in Fig. 7(b) of the calculated spectrum with onsite Coulomb energies and Hund's coupling, we find that $U_{Gd}^{DFT} = 6.5$ eV gives a fair match with experiment. The comparison of soft x-ray PES [Fig. 7(b), same as in Fig. 2(e)] and HAXPES [Fig. 4(c)] valence band spectra allows us to identify the weak feature at about 8.8 eV BE in the soft x-ray PES spectrum to be due to Gd 4*f* surface states, as this feature is missing in bulk sensitive HAXPES spectrum. Further, the average magnetic moment of Gd is calculated
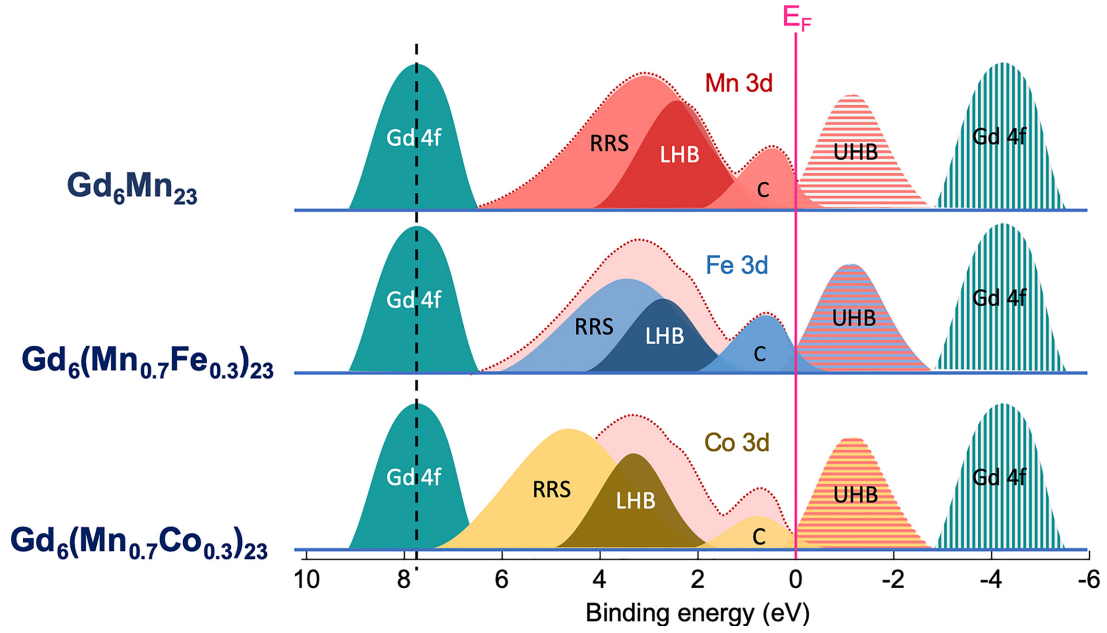
FIG. 8. Schematic of the occupied and unoccupied electronic structure of Gd_6Mn_{23}, $Gd_6(Mn_{0.7}Fe_{0.3})_{23}$, and $Gd_6(Mn_{0.7}Co_{0.3})_{23}$, showing the Mn, Fe, and Co Lower and Upper Hubbard bands (LHB, UHB), the coherent feature (C), the resonant Raman satellite (RRS) feature, and the Gd $4f$ occupied and unoccupied states.

to be $\mu_{Gd} = +7.18\,\mu_B$, in good agreement with the localized Gd^{3+} $4f^7$ configuration. Assuming $J_{ff} = 0.7\,eV$ as is known for Gd metal [68,69], we obtain for Gd_6Mn_{23}, $U_{Gd}^{eff} = U_{ff} + 6J_{ff} = U_{Gd}^{DFT} + 7J_{ff} = 11.4\,eV$. This value is close to the $U_{Gd}^{eff} \approx 11\,eV$ of Gd metal [21], and is expected for the localized Gd $4f$ states in Gd_6Mn_{23}.

In Fig. 8, we have plotted the schematic electronic structure of Gd_6Mn_{23} and how it gets modified by Fe and Co substitution. In particular, we identify the Mn $3d$ occupied and unoccupied states lying between the localized Gd^{3+} occupied and unoccupied states. Further, the Mn $3d$ states split into coherent states at and near E_F and the lower Hubbard band (LHB) of Gd_6Mn_{23} is at 2.7 eV BE. Upon Fe substitution, the Fe $3d$ states lie very close to Mn $3d$ states and essentially exhibit very similar coherent states as well as a lower Hubbard band at slightly higher BE. Moreover, the relative spectral intensities of the coherent states and LHBs in $Gd_6(Mn_{0.7}Fe_{0.3})_{23}$ are also very similar [Fig. 4(a)], suggesting a similar U_{dd}/W, the ratio of onsite Coulomb energy to the coherent band width W. This is borne out by the fact that the Mn and Fe $3d$ states show very similar values of $U_{dd(A)} = 2.1 \pm 0.4\,eV$ and $2.2 \pm 0.4\,eV$. In contrast, with Co substitution, the position of the LHB is at a higher BE and the relative intensity of the Co $3d$ coherent states is lower in $Gd_6(Mn_{0.7}Co_{0.3})_{23}$ [Fig. 4(b)], suggesting stronger correlations which is consistent with the relatively larger $U_{dd(A)} = 2.9 \pm 0.4\,eV$ for Co.

Thus, the lower relative intensity of the $3d$ states at E_F indicate that the effective carrier density is reduced in $Gd_6(Mn_{0.7}Co_{0.3})_{23}$ compared to $Gd_6(Mn_{0.7}Fe_{0.3})_{23}$. This is expected to reduce the specific-heat Sommerfeld coefficient γ in $Gd_6(Mn_{0.7}Co_{0.3})_{23}$ and alter the conductivity significantly compared to $Gd_6(Mn_{0.7}Fe_{0.3})_{23}$. The overall results indicate that the TM onsite Coulomb correlations are mainly responsible for the electronic transport properties derived from the

carriers at E_F, while the more strongly correlated f electron states are situated far from E_F.

IV. CONCLUSIONS

In conclusion, the electronic structure and $3d$ partial density of states of the ferrimagnetic materials $Gd_6(Mn_{1-x}M_x)_{23}$ (M = Fe, Co; $x = 0.0$, 0.3) was investigated using x-ray absorption, soft x-ray, hard-x-ray, resonant photoemission, and constant initial state spectroscopy. We could estimate an average $U_{dd} = 2.1 \pm 0.4\,eV$, $2.2 \pm 0.4\,eV$, and $2.9 \pm 0.4\,eV$ for the Mn $3d$, Fe $3d$, and Co $3d$ states, respectively. The relatively larger U_{dd} for Co compared to Fe $3d$ states results in lower DOS for the coherent feature at E_F and higher DOS in the lower Hubbard band away from E_F in $Gd_6(Mn_{0.7}Co_{0.3})_{23}$ compared to $Gd_6(Mn_{0.7}Fe_{0.3})_{23}$. The DFT+$U$ electronic structure calculations for the parent Gd_6Mn_{23} showed that the calculated Mn magnetic moments are consistent with experiments for $U_{dd} = 1.65\,eV$ and $J_{dd} = 0.9\,eV$. We could also simulate the Gd_6Mn_{23} valence band spectrum to be fairly consistent with the experimentally measured spectrum for $U_{Gd}^{DFT} = 6.5\,eV$ and $J_{ff} = 0.7\,eV$. The results indicate the crucial role of d-d correlations in the presence of large f-f correlations for tuning the electronic structure and magnetic properties of RE-TM intermetallics.

[1] G. R. Stewart, Heavy-fermion systems, Rev. Mod. Phys. **56**, 755 (1984).

[2] T. Mazet, D. Malterre, M. François, C. Dallera, M. Grioni, and G. Monaco, Nonpareil Yb behavior in $YbMn_6Ge_{6-x}Sn_x$, Phys. Rev. Lett. **111**, 096402 (2013).

[3] L. Eichenberger, A. Magnette, D. Malterre, R. Sibille, F. Baudelet, L. Nataf, and T. Mazet, Possible room-temperature signatures of unconventional $4f$-electron quantum criticality in $YbMn_6Ge_{6-x}Sn_x$, Phys. Rev. B **101**, 020408(R) (2020).

[4] G. R. Stewart, Non-Fermi-liquid behavior in d- and f-electron metals, Rev. Mod. Phys. **73**, 797 (2001).

[5] K. N. R. Taylor, Intermetallic rare-earth compounds, Adv. Phys. **20**, 551 (1971).

[6] W. E. Wallace, *Rare Earth Intermetallics* (Academic Press, San Diego, CA, 1973).

[7] S. B. Roy, Magnetocaloric effect in intermetallic compounds and alloys, in *Handbook of Magnetic Materials*, edited by K. H. J. Buschow (North-Holland Publishing Company, Amsterdam, 2014), Vol. 22, pp. 203–316.

[8] X. X. Wang, W. Q. Wang, W. D. Hutchison, F. Su, Y. F. Xue, C. W. Wang, W. Sun, J. M. Cadogan, S. J. Campbell, Z. X. Cheng, and J. L. Wang, Plateau-like magnetocaloric effect in layered intermetallic compounds activated by tripled magnetic cell, Mater. Today Phys. **21**, 100501 (2021).

[9] V. Balaram, Rare earth elements: A review of applications, occurrence, exploration, analysis, recycling, and environmental impact, Geoscience Frontiers **10**, 1285 (2019).

[10] I. A. Campbell, Indirect exchange for rare earths in metals, J. Phys. F: Met. Phys. **2**, L47 (1972).

[11] M. S. S. Brooks, T. Gasche, S. Auluck, L. Nordström, L. Severin, J. Trygg, and B. Johansson, $3d$-$5d$ band magnetism in rare earth-transition metal intermetallics: Total and partial magnetic moments of the RFe_2, (R = Gd-Yb) Laves phase compounds, J. Appl. Phys. **70**, 5972 (1991).

[12] L. Steinbeck, M. Richter, U. Nitzsche, and H. Eschrig, Phys. Rev. B **53**, 7111 (1996).

[13] V. N. Antonov, M. Galli, F. Marabelli, A. N. Yaresko, A. Ya. Perlov, and E. Bauer, Phys. Rev. B **62**, 1742 (2000).

[14] G. I. Miletic and Z. Blazina, J. Solid State Chem. **180**, 604 (2007).

[15] T. Pandey, M.-H. Du, and David S. Parker, Tuning the magnetic properties and structural stabilities of the 2-17-3 magnets $Sm_2Fe_{17}X_3$ (X = C, N) by substituting La or Ce for Sm, Phys. Rev. Appl. **9**, 034002 (2018).

[16] A. Slebarski, J. Goraus, P. Witas, L. Kalinowski, and M. Fijalkowski, Study of d-electron correlations in skutterudite-related $Ce_3M_4Sn_{13}$ (M = Co, Ru, and Rh), Phys. Rev. B **91**, 035101 (2015).

[17] E. Antoniou, G. Sempros, M. Gjoka, C. Sarafidis, H. M. Polatoglou, and J. Kioseoglou, J. Alloys Compd. **882**, 160699 (2021).

[18] M. S. Bahramy, P. Murugan, G. P. Das, and Y. Kawazoe, Phys. Rev. B **81**, 165114 (2010).

[19] P. Sadhukhan, S. W. D'Souza, V. K. Singh, R. S. Dhaka, A. Gloskovskii, S. K. Dhar, P. Raychaudhuri, A. Chainani, A. Chakrabarti, and S. R. Barman, Influence of anti-site disorder and electron-electron correlations on the electronic structure and revelation of surface valence transition in $CeMnNi_4$, Phys. Rev. B **99**, 035102 (2019).

[20] L. V. Pourovskii, J. Boust, R. Ballou, G. Gomez Eslava, and D. Givord, Higher-order crystal field and rare-earth magnetism in rare-earth-Co_5 intermetallics, Phys. Rev. B **101**, 214433 (2020).

[21] J. K. Lang, Y. Baer, and P. A. Cox, Study of the $4f$ and valence band density of states in rare-earth metals. II. Experiment and results, J. Phys. F: Met. Phys. **11**, 121 (1981).

[22] P. Khuntia, P. Peratheepan, A. M. Strydom, Y. Utsumi, K.-T. Ko, K.-D. Tsuei, L. H. Tjeng, F. Steglich, and M. Baenitz, Contiguous $3d$ and $4f$ Magnetism: Strongly correlated $3d$ electrons in $YbFe_2Al_{10}$, Phys. Rev. Lett. **113**, 216403 (2014).

[23] D. van der Marel and G. A. Sawatzky, Electron-electron interaction and localization in d and f transition metals, Phys. Rev. B **37**, 10674 (1988).

[24] T. Bandyopadhyay and D. D. Sarma, Calculation of Coulomb interaction strengths for $3d$ transition metals and actinides, Phys. Rev. B **39**, 3517 (1989).

[25] S. Biermann, A. Dallmeyer, C. Carbone, W. Eberhardt, C. Pampuch, O. Rader, M. I. Katsnelson, and A. I. Lichtenstein, Observation of Hubbard bands in γ-Manganese, Jetp Lett. **80**, 612 (2004).

[26] J. Sanchez-Barriga, J. Braun, J. Minar, I. Di Marco, A. Varykhalov, O. Rader, V. Boni, V. Bellini, F. Manghi, H. Ebert, M. I. Katsnelson, A. I. Lichtenstein, O. Eriksson, W. Eberhardt, H. A. Durr, and J. Fink, Effects of spin-dependent quasiparticle renormalization in Fe, Co, and Ni photoemission spectra: An experimental and theoretical study, Phys. Rev. B **85**, 205109 (2012).

[27] S. Hüfner, S.-H. Yang, B. S. Mun, C. S. Fadley, J. Schafer, E. Rotenberg, and S. D. Kevan, Observation of the two-hole satellite in Cr and Fe metal by resonant photoemission at the $2p$ absorption energy, Phys. Rev. B **61**, 12582 (2000).

[28] M. Zangrando, E. Magnano, A. Nicolaou, E. Carleschi, and F. Parmigiani, Phys. Rev. B **75**, 233402 (2007).

[29] I. I. Mazin, D. J. Singh, M. D. Johannes, and M. H. Du, Unconventional sign-reversing superconductivity in $LaFeAsO_{1-x}F_x$, Phys. Rev. Lett. **101**, 057003 (2008).

[30] K. Kuroki, S. Onari, R. Arita, H. Usui, Y. Tanaka, H. Kontani, and H. Aoki, Unconventional superconductivity originating from disconnected Fermi surfaces in $LaO_{1-x}F_xFeAs$, Phys. Rev. Lett. **101**, 087004 (2008).

[31] I. I. Mazin and J. Schmalian, Pairing symmetry and pairing state in ferropnictides: Theoretical overview, Physica C: Superconduct. **469**, 614 (2009).

[32] V. I. Anisimov, E. Z. Kurmaev, A. Moewes, and I. A. Izyumov, Strength of correlations in pnictides and its assessment by theoretical calculations and spectroscopy experiments, Physica C: Superconductivity **469**, 442 (2009).

[33] I. I. Mazin, Superconductivity gets an iron boost, Nature (London) **464**, 183 (2010).

[34] M. Cini, Density of states of two interacting holes in a solid, Solid State Commun. **20**, 605 (1976).

[35] M. Cini, Two hole resonances in the XVV Auger spectra of solids, Solid State Commun. **24**, 681 (1977).

[36] G. A. Sawatzky, Quasiatomic Auger spectra in narrow-band metals, Phys. Rev. Lett. **39**, 504 (1977).

[37] M. Cini, Comment on quasiatomic Auger Spectra in narrow-band metals, Phys. Rev. B **17**, 2788 (1978).

[38] B. F. DeSavage, R. M. Bozorth, F. E. Wang, and E. R. Callen, Magnetization of the rare-earth manganese compounds R_6Mn_{23}, J. Appl. Phys. **36**, 992 (1965).

[39] H. R. Kirchmayr, Magnetic properties of rare earth manganese compounds, IEEE Trans. Magn. **2**, 493 (1966).

[40] H. R. Kirchmayr, Magnetic properties of the compound series $Y(Mn_xFe_{1-x})_2$ and $Y_6(Mn_xFe_{1-x})_{23}$, J. Appl. Phys. **39**, 1088 (1968).

[41] H. R. Kirchmayr and W. Steiner, Magnetic order of the compound series $RE_6(Fe_{1-x}Mn_x)_{23}$ (RE = Y, Gd), J. Phys. Colloques **32**, C1-665 (1971).

[42] A. Delapalme, J. Déportes, R. Lemaire, K. Hardman, and W. J. James, Magnetic interactions in R_6Mn_{23} rare earth intermetallics, J. Appl. Phys. **50**, 1987 (1979).

[43] F. T. Parker and H. Oesterreiche, Analysis of magnetic interactions and structure in R_6Mn_{23}, Appl. Phys. A **27**, 65 (1982).

[44] H. Nagai, N. Oyama, Y. Ikami, H. Yoshie, and A. Tsujimura, The magnetic properties of psuedo-binary compounds, $Gd(Mn_xFe_{1-x})_2$ and $Gd_6(Mn_xFe_{1-x})_{23}$, J. Phys. Soc. Jpn. **55**, 177 (1986).

[45] H. Nagai, T. Yokoyama, S. Katsuyama, Y. Amako, H. Yoshie, and K. Adachi, The anomalous behaviour of the electrical resistivities of $Gd(Fe, Mn)_2$ and $Gd_6(Fe, Mn)_{23}$, J. Magn. Magn. Mater. **177-181**, 1131 (1998).

[46] P. Lemoine, A. Vernière, T. Mazet, and B. Malaman, Magnetic and magnetocaloric properties of R_6Mn_{23} (R = Y, Nd, Sm, Gd-Tm, Lu) compounds, J. Magn. Magn. Mater. **323**, 2690 (2011).

[47] P. Lemoine, V. Ban, A. Vernière, T. Mazet, and B. Malaman, Magnetocaloric properties of $Gd_6(Mn_{1-x}Fe_x)_{23}$ alloys (x ⩽ 0.2), Solid State Commun. **150**, 1556 (2010).

[48] P. Lemoine, Ph.D. Thesis, Université Henri Poincaré, Nancy (2011).

[49] P. Lemoine, A. Vernière, B. Malaman, and T. Mazet, Magnetic and magnetocaloric properties of $Gd_6(Mn_{1-x}Co_x)_{23}$ compounds (x ⩽ 0.3), J. Alloys Compd. **680**, 612 (2016).

[50] G. Kresse and J. Hafner, *Ab initio* molecular dynamics for liquid metals, Phys. Rev. B **47**, 558 (1993).

[51] G. Kresse and J. Furthmuller, Efficient iterative schemes for *ab initio* total-energy calculations using a plane-wave basis set, Phys. Rev. B **54**, 11169 (1996).

[52] G. Kresse and D. Joubert, From ultrasoft pseudopotentials to the projector augmented-wave method, Phys. Rev. B **59**, 1758 (1999).

[53] S. L. Dudarev, G. A. Botton, S. Y. Savrasov, C. J. Humphreys, and A. P. Sutton, Electron-energy-loss spectra and the structural stability of nickel oxide: An LSDA+U study, Phys. Rev. B **57**, 1505 (1998).

[54] P. L. Dong, L. Ma, X. Zhou, D. Wang, Q. R. Yao, and L. Li, Structural, magnetic, and magnetocaloric effect of $Gd_6(Mn_{1-x}Fe_x)_{23}$ compounds, J. Low Temp. Phys. **195**, 221 (2019).

[55] W. J. James, K. Hardman, W. Yelon, and B. Kebe, Structural and magnetic properties of $Y_6(Fe_{1-x}Mn_x)_{23}$, J. Phys. Colloques **40**, C5-206 (1979).

[56] K. Hardman, J. J. Rhyne, and W. J. James, Magnetic structures of $Y_6(Fe_{1-x}Mn_x)_{23}$ compounds, J. Appl. Phys. **52**, 2049 (1981).

[57] K. A. Gschneidner Jr, V. K. Pecharsky, and A. O. Tsokol, Rep. Prog. Phys. **68**, 1479 (2005).

[58] T. L. Nguyen, T. Mazet, D. Malterre, H. J. Lin, M. Yoshimura, Y. F. Liao, H. Ishii, N. Hiraoka, Y. C. Tseng, and A. Chainani, Hard x-ray photoemission spectroscopy of the ferrimagnetic series $Gd_6(Mn_{1-x}Fe_x)_{23}$, Phys. Rev. B **106**, 045144 (2022).

[59] See Supplemental Material at http://link.aps.org/supplemental/10.1103/PhysRevB.109.035102 for supporting experimental data and details for estimating onsite Coulomb energies.

[60] T. J. Regan, H. Ohldag, C. Stamm, F. Nolting, J. Luning, J. Stohr, and R. L. White, Chemical effects at metal-oxide interfaces studied by x-ray-absorption spectroscopy, Phys. Rev. B **64**, 214422 (2001).

[61] M. C. Biesinger, B. P. Payne, A. P. Grosvenor, L. W. M. Lau, A. R. Gerson, and R. S. C. Smart, Resolving surface chemical states in XPS analysis of first row transition metals, oxides and hydroxides: Cr, Mn, Fe, Co, and Ni, Appl. Surf. Sci. **257**, 2717 (2011).

[62] J. J. Yeh and I. Lindau, Atomic subshell photoionization cross sections and asymmetry parameters: $1 \leqslant Z \leqslant 103$, At. Data Nucl. Data Tables **32**, 1 (1985).

[63] J. Rusz, I. Turek, and M. Divis, Random-phase approximation for critical temperatures of collinear magnets with multiple sublattices: GdX compounds (X = Mg, Rh, Ni, Pd), Phys. Rev. B **71**, 174408 (2005).

[64] D. Paudyal, Y. Mudryk, Y. B. Lee, V. K. Pecharsky, K. A. Gschneidner, Jr., and B. N. Harmon, Understanding the extraordinary magnetoelastic behavior in GdNi, Phys. Rev. B **78**, 184436 (2008).

[65] L. Petit, Z. Szotek, D. Paudyal, A. Biswas, Y. Mudryk, V. K. Pecharsky, and J. B. Staunton, Magnetic structure of selected Gd intermetallic alloys from first principles, Phys. Rev. B **101**, 014409 (2020).

[66] A. Georges, G Kotliar, W. Krauth, and M. J. Rozenberg, Dynamical mean-field theory of strongly correlated fermion systems and the limit of infinite dimensions, Rev. Mod. Phys. **68**, 13 (1996).

[67] V. I. Anisimov, J. Zaanen, and O. K. Andersen, Band theory and Mott insulators: Hubbard *U* instead of Stoner *I*, Phys. Rev. B **44**, 943 (1991).

[68] B. N. Harmon, V. P. Antropov, A. I. Liechtenstein, I. V. Solovyev, and V. I. Anisimov, Calculation of magneto-optical properties for $4f$ systems: LSDA + Hubbard *U* results, J. Phys. Chem. Solids **56**, 1521 (1995).

[69] V. I. Anisimov, F. Aryasetiawan, and A. I. Lichtenstein, First-principles calculations of the electronic structure and spectra of strongly correlated systems: The LDA +U method, J. Phys.: Condens. Matter **9**, 767 (1997).